

OPTICS

Imaging through noise with quantum illumination

T. Gregory, P.-A. Moreau, E. Toninelli, M. J. Padgett*

The contrast of an image can be degraded by the presence of background light and sensor noise. To overcome this degradation, quantum illumination protocols have been theorized that exploit the spatial correlations between photon pairs. Here, we demonstrate the first full-field imaging system using quantum illumination by an enhanced detection protocol. With our current technology, we achieve a rejection of background and stray light of up to 5.8 and also report an image contrast improvement up to a factor of 11, which is resilient to both environmental noise and transmission losses. The quantum illumination protocol differs from usual quantum schemes in that the advantage is maintained even in the presence of noise and loss. Our approach may enable laboratory-based quantum imaging to be applied to real-world applications where the suppression of background light and noise is important, such as imaging under low photon flux and quantum LIDAR.

INTRODUCTION

Conventional illumination uses a spatially and temporally random sequence of photons to illuminate an object, whereas quantum illumination can use spatial correlations between pairs of photons to achieve performance enhancements in the presence of noise and/or losses. This enhancement is made possible by using detection techniques that preferentially select photon-pair events over isolated background events. The quantum illumination (QI) protocol was introduced by Lloyd (1) and generalized to Gaussian states by Tan *et al.* (2), where they proposed a practical version of the protocol. Quantum illumination has applications in the context of quantum information protocols such as secure communication (3, 4) where it secures communication against passive eavesdropping techniques that take advantage of noise and losses. The protocol has also been proposed to be useful for detecting the presence of a target object embedded within a noisy background, despite environmental perturbations and losses destroying the initial entanglement (5–7).

In 2013, Lopaeva *et al.* (8) performed an experimental demonstration of the quantum illumination principle to determine the presence or absence of a semitransparent object by exploiting intensity correlations of a quantum origin in the presence of thermal light. In addition, a quantum illumination protocol has been experimentally demonstrated in the microwave domain (9), and a further demonstration in which joint detection of the signal and idler is not required (10). However, these previous demonstrations were restricted to simply detecting the presence or absence of a target, rather than performing any form of spatially resolved imaging. The acquisition of an image using quantum illumination has recently been reported (11), but that demonstration was performed using a single-transverse-mode source of correlated photon pairs and by raster-scanning the object within one of these single-mode beams. The aforementioned demonstration may be seen as a qualitative assessment of the method, but a full-field imaging implementation of the quantum illumination protocol remains to be demonstrated using a multitransverse-mode source of single photons and spatially resolved coincidence detections. Furthermore, the work in (11) uses only a coherent state as the incoming background light rather than a thermal state as was used in (8). The use of thermal light as the incoming background light, as does the work presented here, better represents

environmental light statistics, and therefore, performing full-field imaging using quantum illumination would be a demonstration of the potential real-world applications of the quantum illumination protocol.

In quantum imaging, commonly used properties are spatial quantum correlations, which can be exploited to surpass the classical limits of imaging (12–16). These quantum correlations have been used in the case of NOON states for enhanced phase detection (17, 18) through the use of definite number of photons to improve the signal-to-noise ratio for measuring the absorption of objects through sub-shot-noise measurements (15, 19–21) and to perform resolution-enhanced imaging by centroid estimation of photon pairs (22). These schemes rely on the ability to detect and use quantum properties after the probed object and are therefore sensitive to decoherence through the introduction of environmental noise and optical losses that lead to severe degradation of the quantum enhancement (23). These schemes are therefore limited to low-noise and high detection efficiency conditions and to the sensing of objects presenting relatively low absorption. These limitations make these schemes difficult to implement in real-world conditions. However, the quantum illumination protocol, as described by Lloyd (1), is resilient to environmental noise and losses.

In this work, we use spatial correlations between downconverted photon pairs to demonstrate the first quantum illumination full-field imaging protocol. The spatial quantum correlations are manifested in the entangled photon pairs produced via spontaneous parametric downconversion (SPDC). The twin beams produced via the SPDC process are directed to different regions of an electron-multiplying charge-coupled device (EMCCD) array detector. EMCCD array detectors have previously been used to measure spatial correlations between photon pairs (24–26). By performing a pixel-by-pixel AND-operation between two regions of an array detector containing the SPDC beams, we preferentially select correlated photon-pair events and reject uncorrelated background light and sensor noise events. As a result of this preferential selection, the quantum illumination AND-image resulting from the sum of these AND-events produces a contrast advantage relative to the classically acquired image comprising the simple sum of the raw events. This relative contrast advantage and background rejection is achieved through the suppression of both background light and sensor noise. We also show that the advantage of the quantum illumination protocol over a classical imaging scheme is maintained in the presence of both noise

Copyright © 2020
The Authors, some
rights reserved;
exclusive licensee
American Association
for the Advancement
of Science. No claim to
original U.S. Government
Works. Distributed
under a Creative
Commons Attribution
License 4.0 (CC BY).

School of Physics and Astronomy, University of Glasgow, Glasgow G12 8QQ, UK.
*Corresponding author. Email: miles.padgett@glasgow.ac.uk

and losses. The quantum advantage that we report is relative to the optimum classical measurement obtained via photon counting and not obtained via any phase-sensitive measurement. This is to perform the demonstration using equivalent experimental conditions to acquire both the classical image and the quantum illumination AND-image in which an identical optical system, illumination source, illumination level, and noise are used to collect data, as it is acquired within the same acquisition. A phase-sensitive detection method (2, 5) would require a different optical setup for the classical acquisition in addition to phase stability, and it would prove impractical to perform imaging in real-world scenarios.

This demonstration of a quantum illumination full-field imaging protocol is an important development in the application of quantum technologies within a real-world setting in which background light and sensor noise require suppression. Applications of quantum illumination protocols such as quantum light detection and ranging (LIDAR) will become more viable as multipixel single-photon avalanche diode (SPAD) arrays that are capable of time-tagging single-photon events are developed. As opposed to the EMCCD camera that we use here, an Andor iXon Ultra 888 with a single-frame acquisition time of ~ 0.015 s for our acquisition parameters (see the Supplementary Materials for full details regarding camera acquisition parameters), the current generation of SPAD arrays being developed have increased acquisition speed and time resolution, with frame rates of 100 kfps and gate times of 4 ns, respectively, being achievable (27). An improvement of around seven orders of magnitude in the temporal resolution of the detector will potentially allow useful depth measurements of a scene to be made.

RESULTS

Imaging system

The experimental configuration is shown in Fig. 1. A 3-mm-thick β -barium borate (BBO) nonlinear crystal cut for type II degenerate downconversion is pumped by a collimated ~ 8 -mm-diameter laser beam at 355 nm to generate SPDC photon pairs centered on the degenerate wavelength of 710 nm. A type II phase-matched down-conversion source results in the spatial separation of the two emitted SPDC beams labeled as the probe beam and the reference beam. The probe beam illuminates the object and may be subject to envi-

ronmental losses and noise, while the reference beam neither interacts with the object nor is it subject to environmental losses and noise. After transmission through the crystal, the pump beam is removed using a pair of dichroic mirrors, and a pair of high-transmission interference filters mounted before the camera select the down-converted photon pairs centered at the degenerate wavelength of 710 nm. As shown in Fig. 1, the target object is placed in the far field of the crystal such that the probe beam interacts with it, while the reference beam has a free optical path. This plane is demagnified by a factor of 8 and imaged onto an EMCCD array detector such that the two downconverted beams are imaged by different regions of the EMCCD array detector of pixel size $13\ \mu\text{m} \times 13\ \mu\text{m}$. The size of the correlations between the probe and reference beam in the far field of the downconversion crystal depends on the wavelength and diameter of the pump beam and the effective focal length of the transform lens (L_1). For the configuration presented here, this gives a correlation width of $\sigma \approx 4\ \mu\text{m}$ in the plane of the EMCCD camera chip. A background light field is deliberately introduced using a thermal light source to illuminate a mask, which overlays the probe beam through a reflection from a microscope slide slip cover (MS) placed in the image plane of the crystal. A thermal light source is used so as to simulate real-world conditions in which environmental noise will follow a similar distribution (i.e., noisier than a Poisson distribution) and be broad-band illumination. The level of demagnification for the quantum imaging arm was set to maximize the number of SPDC photon pairs arriving in anticorrelated detector pixel positions while maintaining the ability to construct an image that is not undersampled. See Materials and Methods for full details regarding optical setup and camera acquisition parameters.

We obtained our results using an illumination regime that was used by Tascia *et al.* (28), in which the threshold events per pixel per frame from the detection of SPDC photons match the event rate due to the noise of the camera, which, for our detector and acquisition settings, is ~ 0.0016 events per pixel per frame over the chosen acquisition region. As discussed above, background thermal illumination was added to the region of the sensor on which the probe beam is detected, thereby simulating environmental noise at the probe beam wavelength, which the quantum illumination protocol is able to reject. Neutral density (ND) filters may be introduced after the target object to introduce optical losses as applied to the probe

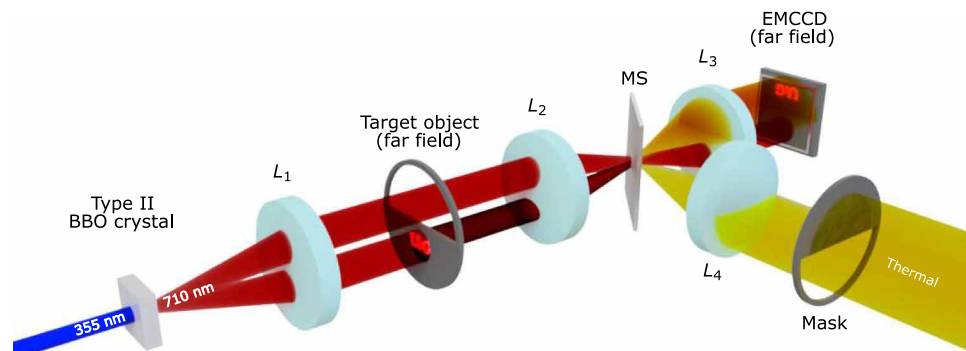


Fig. 1. Schematic of the quantum illumination experimental setup. A BBO crystal cut for type II downconversion is pumped by a ultraviolet laser to produce entangled photon pairs via SPDC. The probe beam interacts with the target object placed in the far field of the crystal, while the reference beam has a free optical path. The lenses $L_1 = 75$ mm, $L_2 = 400$ mm, and $L_3 = 50$ mm comprise the quantum arm optics used to transform into the far field and then to demagnify by a factor of 8 onto the EMCCD camera. A mask illuminated by thermal light is projected onto the camera using lenses $L_4 = 300$ mm and $L_3 = 50$ mm by reflection from the microscope slide slip cover (MS) placed in the image plane of the crystal.

beam to demonstrate the resilience to losses of the quantum illumination protocol.

Image analysis

To take advantage of the quantum illumination, a simple pixel-by-pixel AND-operation between the two regions of the sensor that detect the reference and the probe beams within the same frame is performed. This pixel-by-pixel AND-operation is equivalent to taking the Hadamard product of the two image arrays and is represented in Fig. 2B, where it may be seen that those events that occur in diametrically opposite positions about the correlation peak are added together to build the quantum illumination AND-image. These events are selected by rotating the region of the camera frame corresponding to the probe beam through an angle of π to transform the momentum anticorrelation into a position correlation and then performing the AND-operation to select the pixel coordinates in which an event is detected in both the reference and the probe beam. Performing this operation serves to select the momentum-anticorrelated photon pairs, which comprise the correlation peak presented in Fig. 2A. The result of this software AND-operation over a number of frames is then summed to build the AND-image. The AND-image constructed by summing the result of this pixel-by-

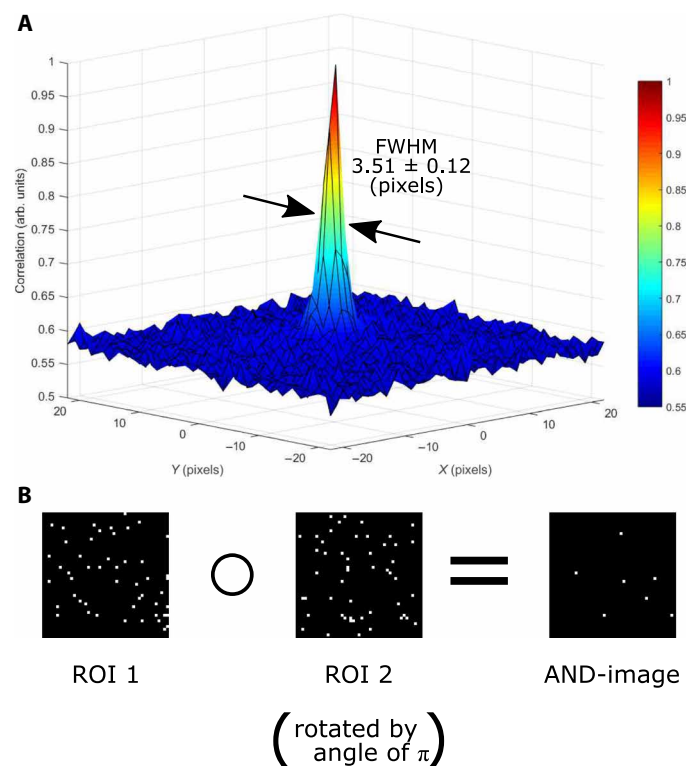


Fig. 2. Cross-correlation. (A) Correlation peak resulting from the cross-correlation of the two regions of interest that comprise the beams containing the photon pairs. The correlation peak was calculated from 250,000 frames under an illumination regime identical to that in which the data were taken. FWHM, full width at half maximum. (B) Representation of the pixel-by-pixel AND-operation on a sum of 10 frames for visualization purposes. Of the two regions of interest that comprise the regions of the frame on which the reference and probe beams are detected [regions of interest (ROIs)], one must be rotated through an angle of π to transform the momentum anticorrelation into a position correlation such that the AND-operation selects the momentum anticorrelated photon pairs.

pixel AND-operation comprises correlated events and shows an improved contrast compared to the classically acquired image which includes both sensor noise events and background illumination events. This advantage is due to the fact that the AND-operation will preferentially keep the photon-pair events and will reject most of the uncorrelated events that arise from either sensor noise or unwanted background illumination.

The number of accidental coincidences between uncorrelated probe and reference events may be reduced by operating in a photon-sparse regime ($\ll 1$ events per pixel per frame). In addition, operating in such a low-light regime may be desirable because of requirements of nonintrusive detection. In the photon-sparse regime under which the system operates ($\ll 1$ events per pixel per frame after thresholding), the intensity correlations between classical beams are extremely weak (8), and therefore, the comparison that we use in this work is between the AND-image obtained using quantum illumination and the direct classical image. Both the AND-image and the classical image are acquired in the same acquisition using an identical optical setup. A general discussion on the optimal operating regimes for QI protocols can be found in (2) and in (8, 15) in the context of photon-counting strategies.

We show that the advantage of the quantum illumination protocol is that it is resilient to thermal background noise and to losses introduced into the probe arm. A theoretical description of the protocol can be found in the Supplementary Materials. To perform a fair analysis of the results, a distinction must be made between the background light and sensor noise, and the noise within the images that is due to shot noise. The quantum illumination AND-images contain fewer events resulting from background light and sensor noise as evidenced by the removal of the cage in Fig. 3 but exhibit greater shot noise \sqrt{n}/n , for which n is the number of events when compared to the classically acquired image. The aim of our quantum illumination protocol is not to demonstrate a signal-to-noise ratio improvement that would rely on sub-shot noise statistics such as that demonstrated by Brida *et al.* (19). Rather, the aim of the quantum illumination protocol presented here is the rejection of background light and sensor noise, which is achieved by the preferential rejection of uncorrelated events under the assumption of an unknown, potentially structured background. As discussed in (15), under the assumption that the background is known or can be independently estimated, the quantum illumination protocol will exhibit an advantage relative to the classically acquired image only when the number of accumulated photons per pixel is relatively low. In the case of an unknown background, it is not possible to algorithmically subtract the background, and as a result, any subtraction applied may confuse or even deliberately mislead an interpretation of the true image.

Rejection of structured thermal illumination

The quantum illumination protocol works with arbitrary structured and a priori unknown environmental background, which illustrates that the quantum illumination protocol works when a lack of knowledge of the background does not permit any ad hoc background subtraction. We demonstrate that this quantum illumination protocol may be used to separate an object illuminated by the probe beam from a mask illuminated with thermal light. In Fig. 3, the bird and the fish are illuminated by the probe beam, and the cage and the net are illuminated by thermal light. By performing the same AND-analysis as previously described on the acquired frames to preferentially reject uncorrelated background light and sensor noise events,

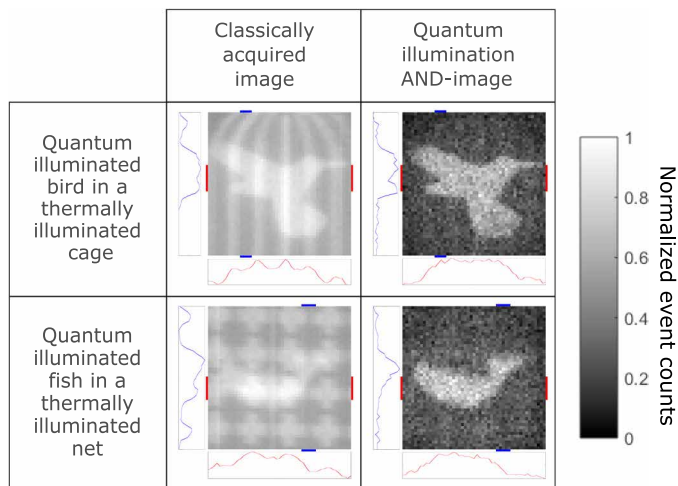


Fig. 3. Images of quantum illuminated target object preferentially selected over thermally illuminated mask. Images of an object under quantum illumination overlaid with a thermally illuminated mask (second column). By applying the AND-operation on the data, the quantum illuminated object may be separated from the thermally illuminated mask (third column). In doing so, the bird may be released from its cage, and the fish may be released from its net. Red lines indicate the rows of the image used to generate the cut graph as shown below the images, while blue lines indicate the columns used to generate the cut graph to the left of the images. Rows and columns used to generate the cut graphs as denoted by the red lines and blue lines, respectively, are rows 19 to 27 and columns 12 to 15 for the bird in a cage and rows 25 to 32 and columns 33 to 37 for the fish in a net. The scale of the cut graphs is normalized intensity (arbitrary units). Images are constructed over 2.5 million frames and are 49×49 pixels.

the quantum-illuminated bird and fish may be distinguished from the thermally illuminated cage and net, respectively.

To assess the distinguishability of the object, we must consider both the image contrast and the signal-to-noise ratio. For a final image comprising the quantum-illuminated target object, of average value, $\langle O \rangle$, above the dark regions of the image and the thermally illuminated structured background, of average value, $\langle S \rangle$, above the dark regions of the image, the rejection of the structured illumination in the form of the cage or net may be characterized as background rejection, $R_{Q/C} = \langle O \rangle / \langle S \rangle$. The rejection ratio, RR , is taken to be the ratio of the values obtained from the quantum illumination AND-image, R_Q , and the classically acquired image, R_C , as per Eq. 1.

$$RR = \frac{R_Q}{R_C} \quad (1)$$

While the above rejection ratio metric assesses the rejection of the thermal background illumination, it does not, however, take into account the shot noise on the quantum-illuminated target object regions (σ_O). This noise (σ_O) will also affect the ability to distinguish the target object (O) from the thermally illuminated structured background (S). We therefore define a figure of merit, $D_{Q/C}$, to take into account the distinguishability of the quantum-illuminated target object (O) against both the thermally illuminated structured background (S) and the noise on the object regions (σ_O) as per Eq. 2.

$$D_{Q/C} = \frac{\langle O \rangle}{\langle S \rangle + \sigma_O} \quad (2)$$

Note that in the limit where a very large number of frames are acquired, and in the assumption that the noise σ_O is purely due to the shot noise, that is $\sigma_O = \sqrt{O}$, the contribution of this noise in both D_C and D_Q vanishes. For the classically acquired image, the limit in which this noise vanishes is under the acquisition of a smaller number of frames than for the quantum illumination AND-image due to a greater number of events being kept per frame. Under the limit of the acquisition of a very large number of frames, the distinguishabilities become equivalent to the respective background rejection, R_C and R_Q , as defined previously. The maximum attainable image distinguishability advantage is therefore given by the reduction ratio, RR , and is achieved when a large number of frames are acquired such that both the classical and quantum images are smooth.

In Fig. 3, alongside the images, horizontal and vertical cuts through the images are displayed in red and blue, respectively. In the graphs referring to the classically acquired images, there exist peaks corresponding to the thermally illuminated cage and net, while in the case of the graphs referring to the quantum illumination AND-images, the prominence of these peaks is greatly reduced because of the preferential rejection of the uncorrelated background noise events. The graphs referring to the quantum illumination AND-image exhibit greater shot noise due to the images containing fewer events than the classically acquired images, and some peaks remain identifiable in the cut graphs because of increased false correlations in local regions with an increased fill factor. For the bird in a cage as shown in Fig. 3, an improvement in the rejection ratio, RR , of a factor of order 4.2 is observed and a value of 1.3 for the distinguishability metric, D_Q/D_C , mainly limited here by the efficiency of our implementation.

Figure 4 displays the bird in a cage under a range of increasing levels of thermal illumination. In all cases, the prominence of the bars is reduced in the quantum illumination AND-image compared with the classically acquired image; however, some structure remains visible as a result of false correlations. The rejection of background and stray light for the images obtained under these illumination conditions as defined by the rejection ratio, RR , increases from 4.2 to 5.8 across as the level of thermal illumination increases. The distinguishability ratio D_Q/D_C , which takes into account the variations within the quantum-illuminated object, is also shown to present an advantage in the case of the quantum illumination AND-image when compared with the classically acquired image. The distinguishability value may also be seen to increase with the increasing thermal illumination of the cage, and this is due to the quantum illumination AND-image not keeping all of the classical cage events, and therefore, D_Q will decrease at a slower rate than D_C for the classically acquired image.

Quantum illumination advantage

Having demonstrated the use of the QI protocol in terms of rejection of background, we now go on to assess the robustness of this quantum illumination protocol under differing loss and thermal noise levels and measure the ability of our QI scheme to reject the background thermal light and sensor noise. Here, we apply an unstructured background so as to simplify the demonstration compared with a structured background as used above. We use the ratio between the contrasts of the quantum illumination AND-image and the classical image. In both cases, image contrast is quantitatively assessed using the Michelson contrast or visibility (V) as represented in Eq. 3, in

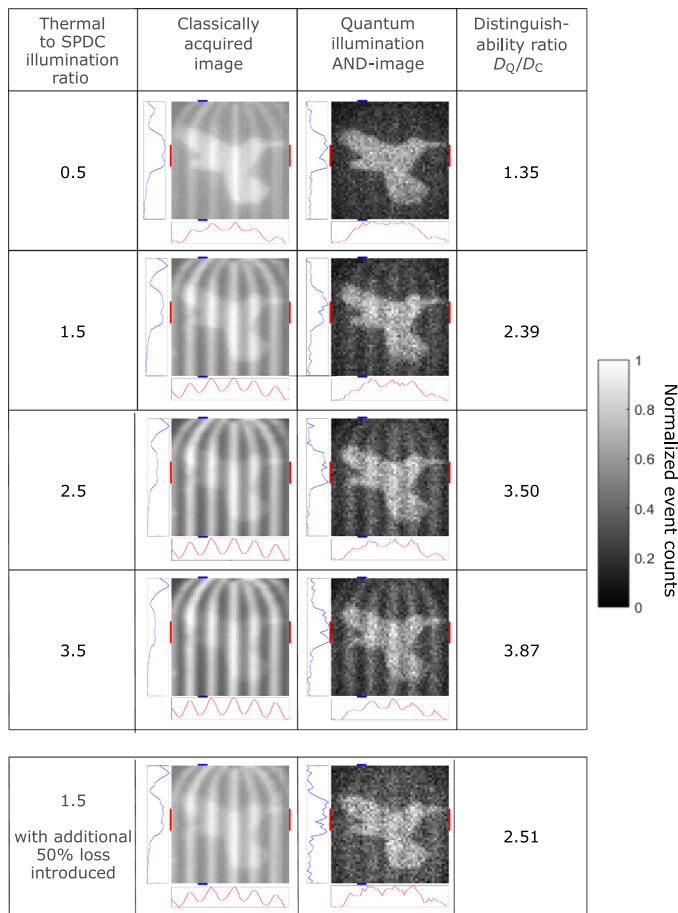


Fig. 4. Images of quantum illuminated target object preferentially selected over thermally illuminated mask with increasing thermal illumination and the introduction of losses. Images of the bird under quantum illumination overlaid with a thermally illuminated cage (second column). By applying the AND-operation on the data, the quantum illuminated bird may be separated from the thermally illuminated cage (third column). In doing so, the bird may be released from its cage. This is demonstrated across a range of increasing levels of thermal illumination represented in the first column as the ratio of the detected average intensity of the thermally illuminated cage image regions to the intensity of the quantum illuminated bird image regions. The final row presents results with the further introduction of ~50% optical losses into the probe beam by way of an ND filter. The distinguishability ratio D_Q/D_C is presented in the fourth column and increases with the increasing thermal illumination of the cage. Red lines indicate the rows of the image used to generate the cut graph as shown below the images, while blue lines indicate the columns used to generate the cut graph to the left of the images. Rows and columns used to generate the cut graphs as denoted by the red lines and blue lines, respectively, are rows 19 to 27 and columns 12 to 15 for the images. The scale of the cut graphs is normalized intensity (arbitrary units). Images are constructed over 2.5 million frames and are 49×49 pixels.

which the difference between the calculated intensities of the bright region (I_{\max}) and the dark region (I_{\min}) of the final summed image is divided by the sum of the intensities in the bright and dark regions.

$$V_{Q/C} = \frac{I_{\max} - I_{\min}}{I_{\max} + I_{\min}} \quad (3)$$

To assess the advantage of the quantum illumination protocol, in this work, we define the quantum illumination advantage, A , as the ratio between the contrast V_Q of the image acquired through quantum illumination (i.e., the image obtained by keeping only the correlated events through performing the AND-operation) and the contrast V_C of the image acquired simply by summing the probe beam events over all frames.

$$A = \frac{V_Q}{V_C} \quad (4)$$

So as to verify that the scheme presented here is a quantum illumination scheme, a binary mask of the University of Glasgow (UoG) initials laser cut from a piece of card was used as the target object. Figure 5 shows a comparison between performing the aforementioned AND-analysis on 1.5 million frames to the corresponding classical image over a range of increasing optical losses introduced into the probe arm of the system by means of a series of ND filters.

From the images presented in Fig. 5, it is seen that the quantum illumination advantage, A , increases with the level of optical losses introduced. This increase in the quantum illumination advantage is due to the fact that the classical image contrast, in which all events are kept, degrades faster than that of the quantum illumination AND-image constructed using the result of the AND-operation (see the Supplementary Materials for a theoretical description of the effect). The quantum illumination advantage also increases with the level of background noise events introduced into the probe beam from a thermal source, as is the expected behavior from the equations that we present in the Supplementary Materials. We also present the corresponding experimental results obtained under increasing levels of thermal illumination introduced into the system in the Supplementary Materials.

In addition to the imaging results for this quantum illumination protocol, we also consider how it may be used in an application where the presence or absence of an object needs to be assessed. This is the context in which Lloyd (1) originally proposed the quantum illumination protocol and has clear applications in realizing quantum LIDAR or quantum radar applications. It can be demonstrated that a strategy combining the information from the classical data and the quantum data, both acquired through quantum illumination, will always lead to a bit error rate enhancement as long as a contrast advantage is detected in the quantum data. This bit error rate enhancement in the context of quantum illumination protocols is discussed in the Supplementary Materials.

DISCUSSION

We have demonstrated a quantum illumination protocol to perform full-field imaging achieving a contrast enhancement through the suppression of both background light and sensor noise. Structure within the thermal background illumination is potentially a priori unknown and therefore cannot be suppressed with a simple ad hoc background subtraction. Through resilience to environmental noise and losses, such a quantum illumination protocol should find applications in real-world implementations including quantum microscopy for low-light level imaging, quantum LIDAR imaging applications, and quantum radar. Improvements in detector technologies such as SPAD arrays capable of time-tagging events should enable time-of-flight applications to be realized and applied outside the laboratory through the increased acquisition speed and time resolution that they enable.

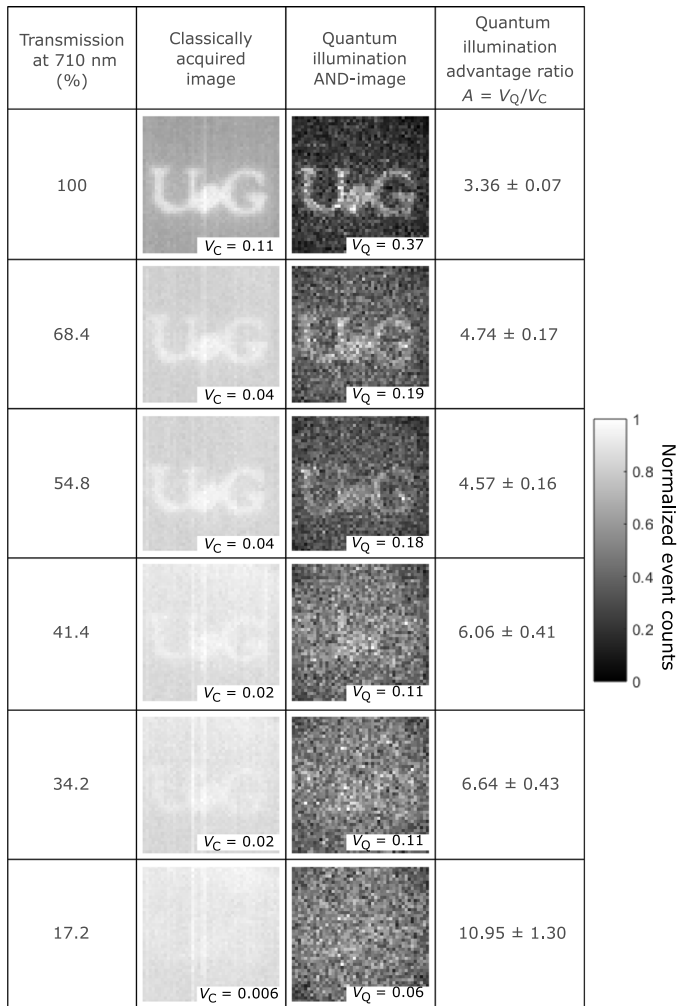


Fig. 5. Imaging using quantum illumination with losses introduced. Imaging using quantum illumination within a thermal background with optical losses introduced. Images of the UoG object with the classical image created by averaging all frames (second column) and the quantum illumination AND-image built from the sum of results of performing an AND-operation to select correlated events in the reference and probe beams (third column). The UoG object illuminated by the probe beam is imaged under the conditions of increasing optical losses (see the transmission of the ND filters placed into the probe beam at 710 nm in the first column). The quantum illumination advantage A under these levels of optical losses for images constructed over 1.5 million frames is displayed in the fourth column. Images are 45×45 pixels.

MATERIALS AND METHODS

The source used for the pump was a JDSU xCyte CY-355-150 Nd:YAG laser with 355-nm output at 160 mW and with a pulse repetition of 100 ± 10 Mhz. The pump was attenuated to ~ 1 mW mm⁻² and expanded to ~ 8 mm on the crystal via a spatial filter comprising a 50-mm lens, a 25- μ m pinhole, and a 200-mm lens. The down-conversion source was a BBO nonlinear crystal of dimensions 10 mm by 10 mm by 3 mm cut for type II degenerate downconversion at 710 nm with a half-opening angle of 5°. The camera used here was an Andor iXon Ultra 888 DU-888 U3-CS0-#BV (100% fill-factor EMCCD camera, with a pixel size of 13 μ m \times 13 μ m). The camera was cooled to -90° C using liquid cooling. Optimal acquisition parameters for the camera were set as follows: vertical speed, 1.33 μ s;

voltage clock amplitude, +0 V, horizontal speed, 10 MHz; electron multiplying (EM) gain, 1000; preamplifier gain set to 1; 128 \times 128 pixel acquisition region; and exposure time of 0.0149500 s (the shortest exposure time for given acquisition parameters).

The filters used in this experiment were Chroma T4551pxt dichroic mirrors (455-nm cutoff and 98% transmission at 710 nm) and Chroma ET710/10 m interference filters (centered on the degenerate wavelength of 710 nm with a bandwidth of 10 nm and a top-hat profile and 99% transmission at 710 nm). Two interference filters were used as degenerate downconversion was not centered on the bandpass thereby resulting in unevenly sized downconversion beams. In addition to having attached one filter directly onto the camera, a second interference filter was inserted into the system and was oriented to shift its transmission profile and to select a narrower overall bandpass and more evenly sized beams.

To each of the frames acquired by the EMCCD camera, a threshold was applied so as to minimize the camera readout noise events that dominate the low values of the analog-digital converter counts histogram for EMCCD cameras while maximizing the overall quantum efficiency of the system. A threshold of $T \approx \mu_{ro} + 3\sigma_{ro}$ is appropriate in which μ_{ro} and σ_{ro} are the mean and standard deviation of the readout noise, respectively. Any frames containing events of an extraordinary nature, taken to be those with pixel values of greater than 45,000, were removed from the dataset because of their containing events caused by cosmic rays striking the detector. See also (21). For the acquisition parameters used here, a threshold of 510 was applied, and this resulted in ~ 0.0016 camera noise events per pixel per frame.

SUPPLEMENTARY MATERIALS

Supplementary material for this article is available at <http://advances.sciencemag.org/cgi/content/full/6/6/eaay2652/DC1>
Supplementary Text
Fig. S1. The quantum illumination advantage as a function of η and T plotted with $d = 0.0016$; $p_r = 0.0016$; $\epsilon = 0.5$.
Fig. S2. The quantum illumination advantage as a function of η and ϵ (plotted with $d = 0.0016$; $p_r = 0.0016$; $T = 0.0016$.
Fig. S3. Imaging using quantum illumination within an increasing thermal background.
Fig. S4. Quantum illumination advantage A calculated over a range of increasing levels of thermal illumination.
Fig. S5. Plot of the quantum illumination advantage A for the system under differing levels of optical loss.
Fig. S6. The bit error rate P_{err} of detecting a target calculated over a range of thermal light levels.
Fig. S7. The bit error rate P_{err} of detecting a target calculated over a range of thermal light levels using the second method.
Table S1. Table of the average s weight values calculated over a range of thermal light levels using the second method for each of the different levels of thermal illumination.

REFERENCES AND NOTES

1. S. Lloyd, Enhanced sensitivity of photodetection via quantum illumination. *Science* **321**, 1463–1465 (2008).
2. S.-H. Tan, B. I. Erkmen, V. Giovannetti, S. Guha, S. Lloyd, L. Maccone, S. Pirandola, J. H. Shapiro, Quantum illumination with Gaussian states. *Phys. Rev. Lett.* **101**, 253601 (2008).
3. J. H. Shapiro, Defeating passive eavesdropping with quantum illumination. *Phys. Rev. A* **80**, 022320 (2009).
4. Z. Zhang, M. Tengner, T. Zhong, F. N. C. Wong, J. H. Shapiro, Entanglements benefit survives an entanglement-breaking channel. *Phys. Rev. Lett.* **111**, 010501 (2013).
5. S. Guha, B. I. Erkmen, Gaussian-state quantum-illumination receivers for target detection. *Phys. Rev. A* **80**, 052310 (2009).
6. S. Pirandola, B. R. Bardhan, T. Gehring, C. Weedbrook, S. Lloyd, Advances in photonic quantum sensing. *Nat. Photonics* **12**, 724–733 (2018).
7. M. Sanz, U. Las Heras, J. Garcia-Ripoll, E. Solano, R. Di Candia, Quantum estimation methods for quantum illumination. *Phys. Rev. Lett.* **118**, 070803 (2017).
8. E. D. Lopaeva, I. R. Berchera, I. P. Degiovanni, S. Olivares, G. Brida, M. Genovese, Experimental realization of quantum illumination. *Phys. Rev. Lett.* **110**, 153603 (2013).

9. S. Barzanjeh, S. Guha, C. Weedbrook, D. Vitali, J. H. Shapiro, S. Pirandola, Microwave quantum illumination. *Phys. Rev. Lett.* **114**, 080503 (2015).
10. C. W. Sandbo Chang, A. M. Vaddiraj, J. Bourassa, B. Balaji, C. M. Wilson, Quantum-enhanced noise radar. *Appl. Phys. Lett.* **114**, 112601 (2019).
11. D. G. England, B. Balaji, B. J. Sussman, Quantum-enhanced standoff detection using correlated photon pairs. *Phys. Rev. A* **99**, 023828 (2019).
12. M. Genovese, Real applications of quantum imaging. *J. Optics* **18**, 073002 (2016).
13. L. A. Lugiato, A. Gatti, E. Brambilla, Quantum imaging. *J. Optics B: Quant. Semiclassical Optics* **4**, S176–S183 (2002).
14. S. P. Walborn, C. H. Monken, S. Padua, P. H. Souto Ribeiro, Spatial correlations in parametric down-conversion. *Phys. Rep.* **495**, 87–139 (2010).
15. A. Meda, E. Losero, N. Samantaray, F. Scafirimuto, S. Pradyumna, A. Avella, I. Ruo-Berchera, M. Genovese, Photon-number correlation for quantum enhanced imaging and sensing. *J. Optics* **19**, 094002 (2017).
16. P.-A. Moreau, E. Toninelli, T. Gregory, M. J. Padgett, Imaging with quantum states of light. *Nat. Rev. Phys.* **1**, 367–380 (2019).
17. V. Giovannetti, S. Lloyd, L. Maccone, Quantum-enhanced measurements: Beating the standard quantum limit. *Science* **306**, 1330–1336 (2004).
18. T. Ono, R. Okamoto, S. Takeuchi, An entanglement-enhanced microscope. *Nat. Commun.* **4**, 2426 (2013).
19. G. Brida, M. Genovese, I. R. Berchera, Experimental realization of sub-shot-noise quantum imaging. *Nat. Photonics* **4**, 227–230 (2010).
20. P.-A. Moreau, J. Sabines-Chesterking, R. Whittaker, S. K. Joshi, P. M. Birchall, A. McMillan, J. G. Rarity, J. C. F. Matthews, Demonstrating an absolute quantum advantage in direct absorption measurement. *Sci. Rep.* **7**, 6256 (2017).
21. E. Toninelli, M. P. Edgar, P.-A. Moreau, G. M. Gibson, G. D. Hammond, M. J. Padgett, Sub-shot-noise shadow sensing with quantum correlations. *Opt. Express* **25**, 21826–21840 (2017).
22. E. Toninelli, P.-A. Moreau, T. Gregory, A. Mihalyi, M. P. Edgar, N. Radwell, M. J. Padgett, Resolution-enhanced quantum imaging by centroid estimation of biphotons. *Optica* **6**, 347–353 (2019).
23. V. Giovannetti, S. Lloyd, L. Maccone, Advances in quantum metrology. *Nat. Photonics* **5**, 222–229 (2011).
24. P.-A. Moreau, J. Mougin-Sisini, F. Devaux, E. Lantz, Realization of the purely spatial Einstein-Podolsky-Rosen paradox in full-field images of spontaneous parametric down-conversion. *Phys. Rev. A* **86**, 010101 (2012).
25. M. P. Edgar, D. S. Tasca, F. Izdebski, R. E. Warburton, J. Leach, M. Agnew, G. S. Buller, R. W. Boyd, M. J. Padgett, Imaging high-dimensional spatial entanglement with a camera. *Nat. Commun.* **3**, 984 (2012).
26. H. Defienne, M. Reichert, J. W. Fleischer, General model of photon-pair detection with an image sensor. *Phys. Rev. Lett.* **120**, 203604 (2018).
27. I. Gyongy, N. Calder, A. Davies, N. A. W. Dutton, R. R. Duncan, C. Rickman, P. Dalgarno, R. K. Henderson, A 256 × 256, 100-kfps, 61% fill-Factor SPAD image sensor for time-resolved microscopy applications. *IEEE Trans. Electron Dev.* **65**, 547–554 (2018).
28. D. S. Tasca, M. P. Edgar, F. Izdebski, G. S. Buller, M. J. Padgett, Optimizing the use of detector arrays for measuring intensity correlations of photon pairs. *Phys. Rev. A* **88**, 013816 (2013).

Acknowledgments

Funding: This work was funded by the UK EPSRC (QuantIC EP/M01326X/1) and the ERC (TWISTS, grant no. 340507). T.G. acknowledges the financial support from the EPSRC (EP/N509668/1) and the Professor Jim Gatheral Quantum Technology Studentship. P.-A.M. acknowledges the support from the European Union Horizon 2020 research and innovation program under the Marie Skłodowska-Curie fellowship grant agreement no. 706410, the Leverhulme Trust through the Research Project Grant ECF-2018-634, and the Lord Kelvin Adam Smith Leadership Fellowship Scheme. E.T. acknowledges the financial support from the EPSRC Centre for Doctoral Training in Intelligent Sensing and Measurement (EP/L016753/1). **Author contributions:** M.J.P. and P.-A.M. conceptualized the project. P.-A.M. and M.J.P. supervised the project. T.G., P.-A.M., E.T., and M.J.P. devised and implemented the project methodology. T.G., E.T., and P.-A.M. performed the experimental investigation. T.G. and E.T. wrote the software to perform the experiment. All authors performed formal analysis of the results and wrote and revised the manuscript. **Competing interests:** The authors declare that they have no competing or noncompeting financial interests. **Data and materials availability:** All data needed to evaluate the conclusions in the paper are present in the paper and/or the Supplementary Materials. Additional data related to this paper may be requested from the authors.

Submitted 5 June 2019

Accepted 21 November 2019

Published 7 February 2020

10.1126/sciadv.aay2652

Citation: T. Gregory, P.-A. Moreau, E. Toninelli, M. J. Padgett, Imaging through noise with quantum illumination. *Sci. Adv.* **6**, eaay2652 (2020).

Imaging through noise with quantum illumination

T. Gregory, P.-A. Moreau, E. Toninelli and M. J. Padgett

Sci Adv **6** (6), eaay2652.

DOI: 10.1126/sciadv.aay2652

ARTICLE TOOLS

<http://advances.sciencemag.org/content/6/6/eaay2652>

SUPPLEMENTARY MATERIALS

<http://advances.sciencemag.org/content/suppl/2020/02/03/6.6.eaay2652.DC1>

REFERENCES

This article cites 28 articles, 2 of which you can access for free
<http://advances.sciencemag.org/content/6/6/eaay2652#BIBL>

PERMISSIONS

<http://www.sciencemag.org/help/reprints-and-permissions>

Use of this article is subject to the [Terms of Service](#)

Science Advances (ISSN 2375-2548) is published by the American Association for the Advancement of Science, 1200 New York Avenue NW, Washington, DC 20005. The title *Science Advances* is a registered trademark of AAAS.

Copyright © 2020 The Authors, some rights reserved; exclusive licensee American Association for the Advancement of Science. No claim to original U.S. Government Works. Distributed under a Creative Commons Attribution License 4.0 (CC BY).